North Atlantic tropical cyclone activity promotes enhanced sea ice in the Kara-Laptev Seas

Liangying Zeng,[1,2] Yao Ha,[1,2,5,*] Chuanfeng Zhao,[4] Jinfeng Ding,[1] Haixia Dai,[1,2] Yimin Zhu,[1,2,5] Yijia Hu,[1,2] and Zhong Zhong[3,5,*]
*Correspondence: hayao1986@yeah.net, hayao86@nudt.edu.cn (Y.H.); zhong_zhong@yeah.net (Z.Z.)
Received: July 9, 2025; Accepted: November 28, 2025; Published Online: January 4, 2026; https://doi.org/10.59717/j.xinn-geo.2026.100190

GRAPHICAL ABSTRACT

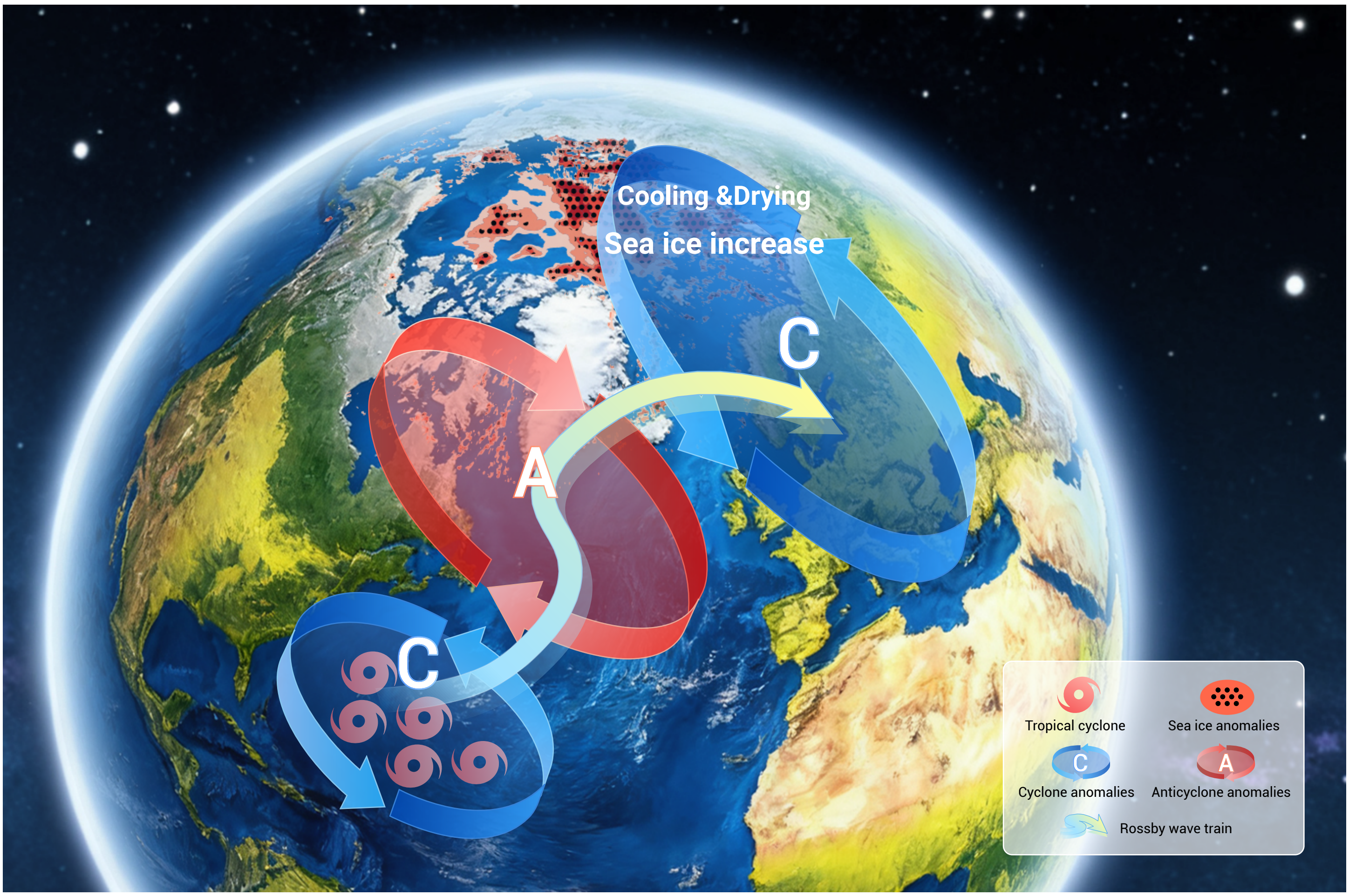

PUBLIC SUMMARY

- North Atlantic tropical cyclone (TC) activity is linked to more October sea ice in the Kara-Laptev Seas (KLS).
- TCs excite poleward-propagating Rossby waves, which induce an anomalous cyclonic circulation over the KLS.
- This cyclonic anomaly suppresses warming and reduces humidity, creating conditions favoring sea ice growth.

North Atlantic tropical cyclone activity promotes enhanced sea ice in the Kara-Laptev Seas

Liangying Zeng,[1,2] Yao Ha,[1,2,5,*] Chuanfeng Zhao,[4] Jinfeng Ding,[1] Haixia Dai,[1,2] Yimin Zhu,[1,2,5] Yijia Hu,[1,2] and Zhong Zhong[3,5,*]

[1]College of Meteorology and Oceanography, National University of Defense Technology, Changsha 410073, China

[2]Key Laboratory of High Impact Weather, China Meteorological Administration, Changsha 410073, China

[3]State Key Laboratory of Climate System Prediction and Risk Management, Nanjing Normal University, Nanjing 210023, China

[4]Department of Atmospheric and Oceanic Sciences, and China Meteorological Administration Tornado Key Laboratory, Peking University, Beijing 100871, China

[5]Jiangsu Collaborative Innovation Center for Climate Change, School of Atmospheric Sciences, Nanjing University, Nanjing 210023, China

*Correspondence: hayao1986@yeah.net, hayao86@nudt.edu.cn (Y.H.); zhong_zhong@yeah.net (Z.Z.)

Received: July 9, 2025; Accepted: November 28, 2025; Published Online: January 4, 2026; https://doi.org/10.59717/j.xinn-geo.2026.100190

Citation: Zeng L., Ha Y., Zhao C., et al. (2026). North Atlantic tropical cyclone activity promotes enhanced sea ice in the Kara-Laptev Seas. *The Innovation Geoscience* **4**:100190.

This study investigates the teleconnection mechanism linking North Atlantic (NA) tropical cyclone (TC) activity to sea ice change in the Kara-Laptev Seas (KLS). Observational analyses indicate significant positive correlations between accumulated cyclone energy over the NA in late September and KLS sea ice concentration in October. It shows that the enhanced NA TC activity excites northeastward-propagating Rossby wave trains via local diabatic heating anomalies, and the wave propagation induces a characteristic upper-tropospheric circulation anomaly pattern, featuring sequential cyclonic, anticyclonic, and cyclonic anomalies over the NA, Greenland and the European sector extending to the KLS, respectively. The cyclonic anomaly over the KLS suppresses adiabatic warming and reduces specific humidity, fostering colder and drier conditions conducive to sea ice growth. Simulations with Community Atmosphere Model version 6 (CAM6) can replicate the teleconnection pathway as well as the observed anomalous circulation structure and planetary-scale Rossby wave propagation. These findings imply that NA TC activity can act as a previously underappreciated contributor to sea ice change over KLS and advance understanding of tropical-Arctic teleconnections.

INTRODUCTION

Satellite monitoring since 1979 has shown accelerated melting of Arctic sea ice, with summer months experiencing the most notable decline.[1,2] The Kara-Laptev Seas (KLS) are often termed the "ice factory" of the Arctic owing to their substantial contribution to sea ice production during the freezing season from October to February.[3] Compared with other Arctic regions, the KLS exhibits greater interannual variability in winter sea ice growth, which has been dominated by thermodynamic growth and increasingly essential dynamic growth under ongoing Arctic warming.[4,5] The KLS is an essential area for ice-atmosphere interactions,[6] and the sea ice change there not only influences local thermodynamic and dynamic conditions but also generates complex climate effects on mid- and low-latitude regions via intricate interaction and feedback mechanisms.[7–9] For instance, diminished autumn KLS sea ice contributes to intensified winter Ural blocking events and the Siberian High, ultimately inducing pronounced cold anomalies across Eurasian regions.[10–12] Furthermore, recent studies have indicated that KLS sea ice anomalies can also have a significant impact on tropical air-sea coupling systems, including El Niño-Southern Oscillation (ENSO),[13,14] Indian Ocean Dipole (IOD)[15] and tropical cyclone (TC) activity,[16] which may be mediated through atmospheric and oceanic feedbacks. These emphasize the significance of the KLS in understanding Arctic and extra-Arctic feedbacks, highlighting the necessity to characterize dominant drivers of its sea ice variability.

Growing evidences reinforce the pivotal role of tropical forcing in modulating Arctic climate and sea ice through tropical-Arctic atmospheric linkages.[17–19]. Typical El Niño events drive sea ice retreat in the Chukchi-Beaufort sector through regional Ferrel cell adjustments,[20,21] whereas central Pacific El Niño enhances Arctic westerlies, slowing Canada Basin summer sea ice melt.[22] Enhanced winter sea ice variability in the Barents-Kara Seas is mediated by ENSO-induced Walker circulation adjustments, with La Niña intensifying Atlantic heat/moisture transport through strengthened Hadley circulation and persistent North Atlantic Oscillation-like patterns that drive ice loss, contrasting with El Niño's suppression of energy transport and subsequent ice retention.[23] It is also found that the positive summer Asian-Pacific Oscillation phases trigger autumn eastern Arctic ice loss through North Atlantic (NA) warming, sustained Barents-Kara-Laptev anticyclones, and enhanced humidity-temperature feedbacks.[24] Concurrently, the NA Sea Surface Temperature (SST) anomalies modulate Barents Sea ice cover through both the Atlantic oceanic heat transport[25,26] and atmospheric moisture pathways.[27] So far, most of the discovered tropical-Arctic connections are mediated by planetary-scale Rossby wave trains.[28–31] These mechanisms collectively deepen our understanding of the Arctic climate responses to tropical forcing.

TCs can act as Rossby wave sources,[32,33] stimulating Rossby waves whose propagation direction depends on the background flow, TC latitude, and potential vorticity structure,[34–36] inducing downstream teleconnections that modulate extratropical weather systems.[37–40] Western North Pacific (WNP) TCs can cause Arctic anomalous cyclonic via Rossby wave poleward propagation, enhancing sea ice over the Arctic-Pacific sector through thermodynamic and dynamic feedbacks,[41] and eastern North Pacific TC activity promotes sea ice increase in the Canadian Basin by triggering large-scale meridional circulation anomalies.[42] Climate projections indicate future intensification of the NA TC activity under greenhouse forcing, featuring distinct spatial shifts - eastward expansion and northward migration.[43,44] Scoccimarro et al. explicitly identified that the acceleration of Transpolar Drift driven by the NA TC activity enhances Beaufort Sea ice export.[45] Besides, it is seen that there may also be an unexamined positive correlation between the NA TC activity and the Kara Sea ice. This spatial difference in sea ice response highlights the complexity of the NA TC activity and Arctic sea ice interaction and demands a deeper investigation. Despite growing recognition of TC-Arctic sea ice interactions, mechanistic understanding remains disproportionately focused on Arctic-Pacific sectors, leaving critical knowledge gaps regarding NA TC impacts on Kara-Laptev "ice factory" regions and associated thermodynamic drivers.

MATERIALS AND METHODS

Data

This study investigates the teleconnection between the NA TC activity and KLS sea ice concentration (SIC) from 1982 to 2020. TC track and intensity data, essential for computing Accumulated Cyclone Energy (ACE), are obtained from the International Best Track Archive for Climate Stewardship (IBTrACS).[46,47] High-resolution daily and monthly SIC records (0.25° × 0.25°) are sourced from the NOAA Optimum Interpolation SST V2 dataset.[48] Meteorological variables, including temperature, zonal/meridional winds, geopotential height, and specific humidity, are acquired from the ERA5 reanalysis,[49] which provides global atmospheric fields at 0.25° spatial resolution. To account for any potential El Niño–Southern Oscillation (ENSO) influences, daily and monthly Niño 3.4 indices from the Hadley Centre Sea Ice and SST (HadISST) dataset are incorporated.[50] Linear trends are removed from all data in this study before statistical analyses.

Accumulated cyclone energy quantification

The daily ACE index quantifies TC activities within a 2° × 2° grid cell by summing the squares of the maximum sustained surface wind speeds (V_i, in m s^{-1}) for all TCs occurring in that cell during a 24-hour period. The ACE index is expressed as,

$$\mathrm{ACE} = \sum_j V_j^2 \quad (1)$$

Here, j denotes the j-th TC within the grid cell during the study day, and V is its corresponding maximum sustained surface wind speed. During the study period, a year is classified as a strong NA ACE year if its normalized value exceeds the climatological mean (1982–2020) NA ACE index by +0.5σ (standard deviation), whereas it is categorized as a weak NA ACE year if the value falls below −0.5σ.

Correlation analysis

The linear relationship between the variables ACE and SIC is quantified using the Pearson correlation coefficient (r). To address potential confounding effects of ENSO on the relationship between the NA TC activity and the KLS SIC, partial correlation analysis is applied, controlling for the Niño 3.4 index. This method isolates the direct association between two variables while removing the influence of a third variable.[51,52] The partial correlation coefficient $r_{XY,Z}$ between variable X and variable Y, adjusted for variable Z, is defined as,

$$r_{XY,Z} = \frac{r_{XY} - r_{XZ} r_{YZ}}{\sqrt{(1 - r_{XZ}^2)(1 - r_{YZ}^2)}} \quad (2)$$

Here, r_{XY}, r_{XZ} and r_{YZ} stands for the Pearson correlation coefficients between the respective variable pairs.

All regression models incorporated the preceding September ENSO signal removal, which is synchronous with ACE, through linear regression. The adjusted variable ξ^* is expressed as,[53,54]

$$\xi^* = \xi - Niño3.4 \times \frac{cov(\xi, Niño3.4)}{var(\xi)} \quad (3)$$

where refers to the original field, the $cov(\xi, Niño3.4)$ represents the covariance between the original field and Niño 3.4 index, $var(\xi)$ represents the variance of the original field.

Rossby waves diagnosis

To diagnose the propagation mechanisms of Rossby waves, this study employs 3D Plumb wave activity flux, which can capture zonal, meridional, and vertical wave propagation of quasi-stationary waves, and is defined as,[55]

$$\boldsymbol{F}_s = p\cos\varphi \times \begin{pmatrix} v'^2 - \dfrac{1}{2\Omega a \sin 2\varphi}\dfrac{\partial(v'\Phi')}{\partial\lambda} \\ -u'v' + \dfrac{1}{2\Omega a \sin 2\varphi}\dfrac{\partial(u'\Phi')}{\partial\lambda} \\ \dfrac{f}{S}\left[v'T' - \dfrac{1}{2\Omega a \sin 2\varphi}\dfrac{\partial(T'\Phi')}{\partial\lambda}\right] \end{pmatrix} \quad (4)$$

where $p, \varphi, \lambda, \Phi$ denote pressure, latitude, longitude, and geopotential height, respectively. f is the Coriolis parameter. a is the radius of Earth. Ω is the Earth's rotation rate. u, v, T represent zonal wind, meridional wind and temperature, respectively. Primes denote the deviations from zonal means. $S = \partial\tilde{T}/\partial z + \tilde{T}/H$ is the static stability, where $\kappa \approx 0.286$ is the ratio of the specific gas constant of dry air to the specific heat of dry air. $\tilde{T}$ represents the domain average of temperature and H is the log-pressure scale height. $z = -Hlnp$ is the vertical coordinate.

The Rossby Wave Source (RWS), a key driver of Rossby wave generation, is defined as the combined effect of vorticity advection and divergent flow,[56,57]

$$RWS = -\zeta D - \boldsymbol{v}_\chi \cdot \nabla\zeta = -\nabla \cdot (\boldsymbol{v}_\chi \zeta) \quad (5)$$

where denotes absolute vorticity, D is the horizontal divergence, and $\boldsymbol{v}$ refers to the divergent component derived from velocity potential. The RWS helps quantify localized forcing mechanisms, such as barotropic instability from shear flows or baroclinic instability from density gradients, which are essential for initiating and sustaining Rossby waves.

Liang-Kleeman information flows analysis

Correlation analysis alone cannot establish causality as statistically significant linkages may arise from indirect interactions or shared external forcings. The Liang-Kleeman information flow $T_{2\to1}$ represents the rate of information transfer from variable X_2 (NA ACE) to X_1 (KLS SIC) per unit time, calculated via a linear model as:[58]

$$T_{2\to1} = \frac{C_{11}C_{12}C_{2,d1} - C_{12}^2 C_{1,d1}}{C_{11}^2 C_{22} - C_{11}C_{12}^2} \quad (6)$$

In this formula, X_2 and X_1 mark two time series, and $T_{2\to1}$ stands for the directional information flows from series X_2 to X_1. The term C_{ij} quantifies the covariance between the respective time series, while $C_{i,dj}$ represents the covariance between time series X_i and the discrete time derivative $\Delta X_j/\Delta t$. A value $T_{2\to1} = 0$ indicates no causal influence from X_2 to X_1, while non-zero values (positive or negative) reflect directional causality, with magnitude proportional to the strength of information transfer.

Singular value decomposition for covariance mode extraction

To identify dominant coupled variability patterns between the NA ACE index and KLS SIC, singular value decomposition (SVD), also termed maximum covariance analysis (MCA), is applied. This method decomposes the cross-covariance matrix of the paired datasets, isolating orthogonal spatial modes and their associated temporal coefficients that maximize covariance between the NA ACE and KLS SIC. The leading SVD modes can reveal synchronized spatial structures and phase-lagged temporal evolution.[59,60]

Sensitivity experiments with the atmospheric model

To elucidate causal mechanisms connecting the NA TC activity to KLS sea ice variability, we perform atmospheric sensitivity experiments using the Community Atmosphere Model version 6 (CAM6) in a standalone configuration.[61] The model configuration employs 32 vertical hybrid sigma-pressure layers (surface to 3.6 hPa) and a 0.9° × 1.25° horizontal grid. Two simulations are designed to diagnose the possible effects of the NA TC activity on the Arctic atmosphere. The control simulation (CTRL) adopts the F2000climo component set with year 2000 external forcing (representing the 1982–2020 climatology). It is initialized on 21st September 2000 and integrated for two months. The perturbed simulation (ANOM) is identical to CTRL but additionally superimposes observed sea level pressure (SLP) anomalies over the NA (5–50°N, 20–70°W). These SLP anomalies are derived from the composite difference between strong and weak ACE years during late September (21st-30th) for the 1982–2020 period. Comparison of the differences between ANOM and CTRL experiments allows the Arctic atmospheric response to the NA TC activities to be obtained. Both simulations include 20 ensemble members with initial temperature perturbations sequentially scaled from 1×10^{-14} (member 1) to 20×10^{-14} (member 20), generated via the stochastic parameterization.

RESULTS

Observed spatiotemporal linkage between the NA TC activity and sea ice over the KLS

The 10 day-to-10 day lead-lag correlation between North Atlantic (NA; 5–50°N, 20–70°W) accumulated cyclone energy (ACE) and Kara-Laptev Seas (KLS; 70–85°N, 60–160°E) sea ice concentration (SIC) during late summer to early autumn (August–October) is shown in Figure 1, as this period represents a critical phase for sea ice growth and NA TC activity reaches its climatological peak. The NA ACE index in late September (21st–30th) demonstrates robust positive correlations with the KLS SIC with a lag of 10-40 days. This indicates that the NA TC activity in late September makes a significant positive contribution to KLS SIC throughout October. Notably, these positive correlations peak in mid-October (11th–20th) with a correlation coefficient of 0.46 ($p < 0.01$), suggesting a lag of about 20 days for the strongest influence from the tropics. Conversely, no significant associations emerge between the KLS SIC of 0–60-day lead and the NA ACE index in late September, indicating that the KLS sea ice changes are a response rather than a precursor to the NA TC activity. Based on this time scale, it is conjectured that lagged changes in the Arctic sea ice may be related to teleconnection from the tropics. These phased relationships persist after the ENSO signal is removed,

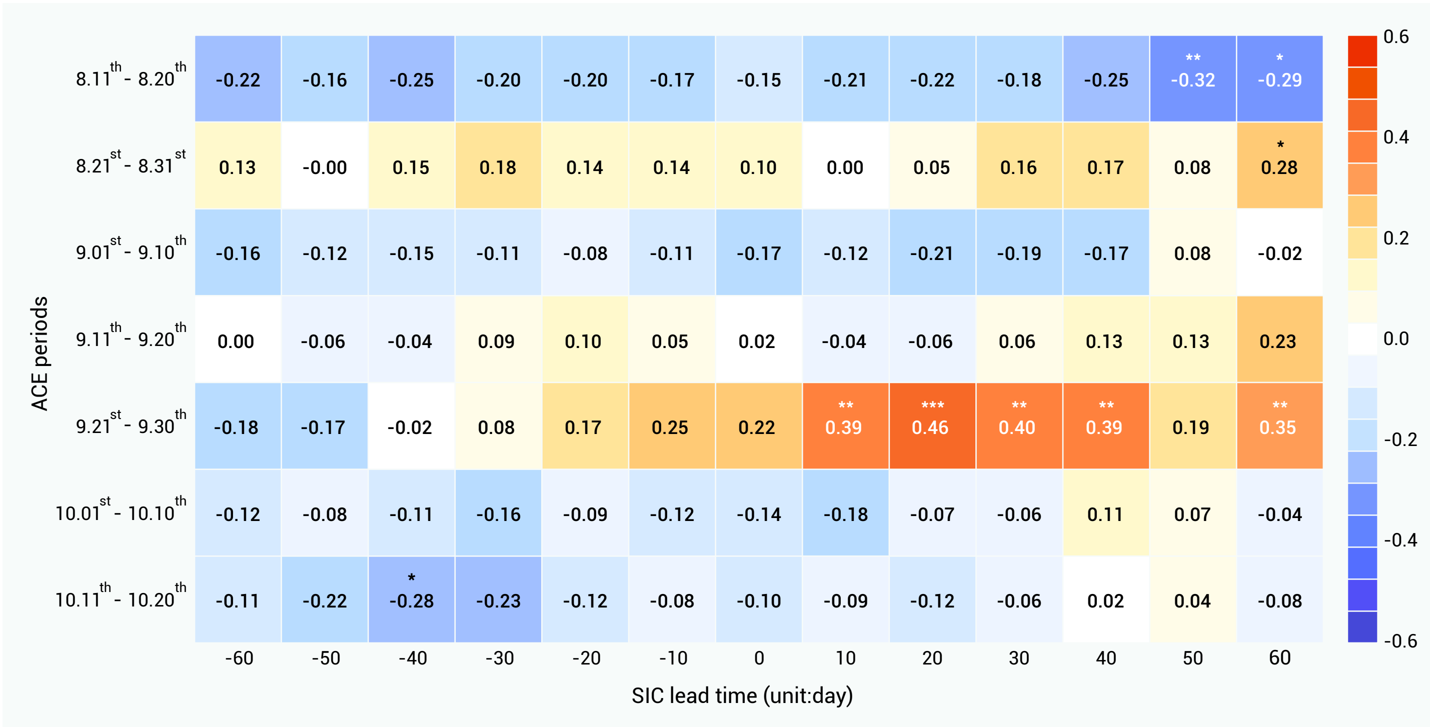

Figure 1. The 10 day-to-10 day lead-lag correlations between the accumulated cyclone energy (ACE) over the North Atlantic (NA) and sea ice concentration (SIC) over the Kara-Laptev Seas (KLS) for 1982–2020 The symbols "*", "**", and "***" above the correlation value indicate statistical significance based on a two-tailed Student's *t*-test at confidence levels of 90%, 95%, and 99%, respectively. For example, the value ***0.46 in row 5, column 9 represents the correlation coefficient between the NA ACE in late September (September 21st–30th) and the KLS SIC in mid-October (October 11th–20th; with a lag of 20 days), which is statistically significant at the 99% confidence level.

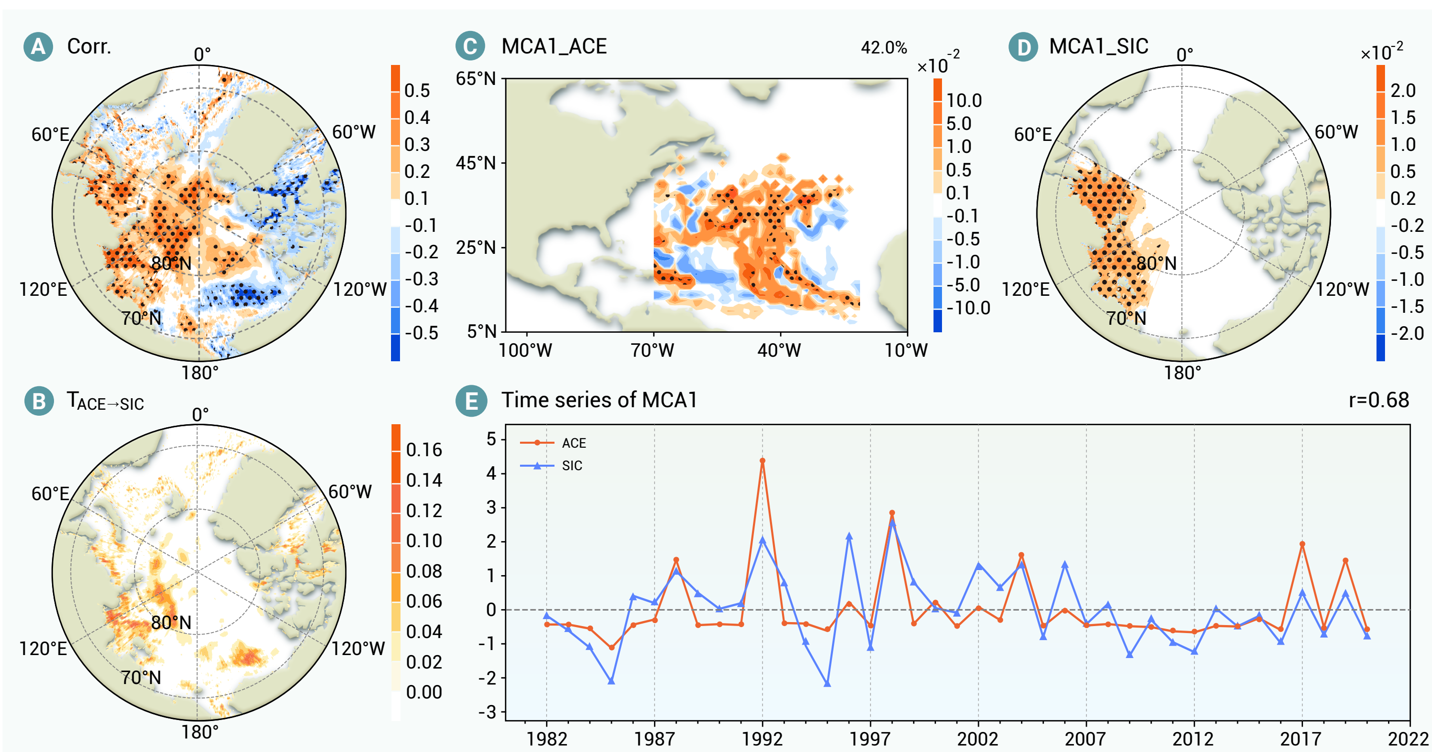

Figure 2. The spatial correlation and maximum covariance analysis of accumulated cyclone energy (ACE) and sea ice concentration (SIC) (A) The spatial pattern of partial correlation coefficients (shading) for removing ENSO in September between the detrended North Atlantic (NA, 5–50°N, 20–70°W) averaged ACE in late September and October SIC over the Arctic. (B) Absolute value of the Liang-Kleeman information flow (shading, unit: nats per 20-day) from the NA ACE in late September to the Arctic SIC in October. The principal mode of maximum covariance analysis between detrended (C) late September ACE in the NA and (D) October SIC in the Kara-Laptev Seas (KLS, 70–85°N, 60–160°E) and (E) their corresponding time series from 1982 to 2020. The principal mode accounts for 42.0% of the covariance, and the correlation coefficient between the time series of the NA ACE and KLS SIC is 0.68 ($p < 0.01$). The dotted regions in (A), (C) and (D) indicate statistical significance based on a two-tailed Student's *t*-test at the 90% confidence level.

further supporting the robustness of TC activity in mediating KLS SIC adjustments.

Figure 2 depicts robust teleconnections between the NA ACE in late September and the KLS SIC in October. Spatial correlation analysis reveals statistically significant positive linkages between the NA ACE in late September and the KLS SIC in October, with the strongest positive correlation mainly

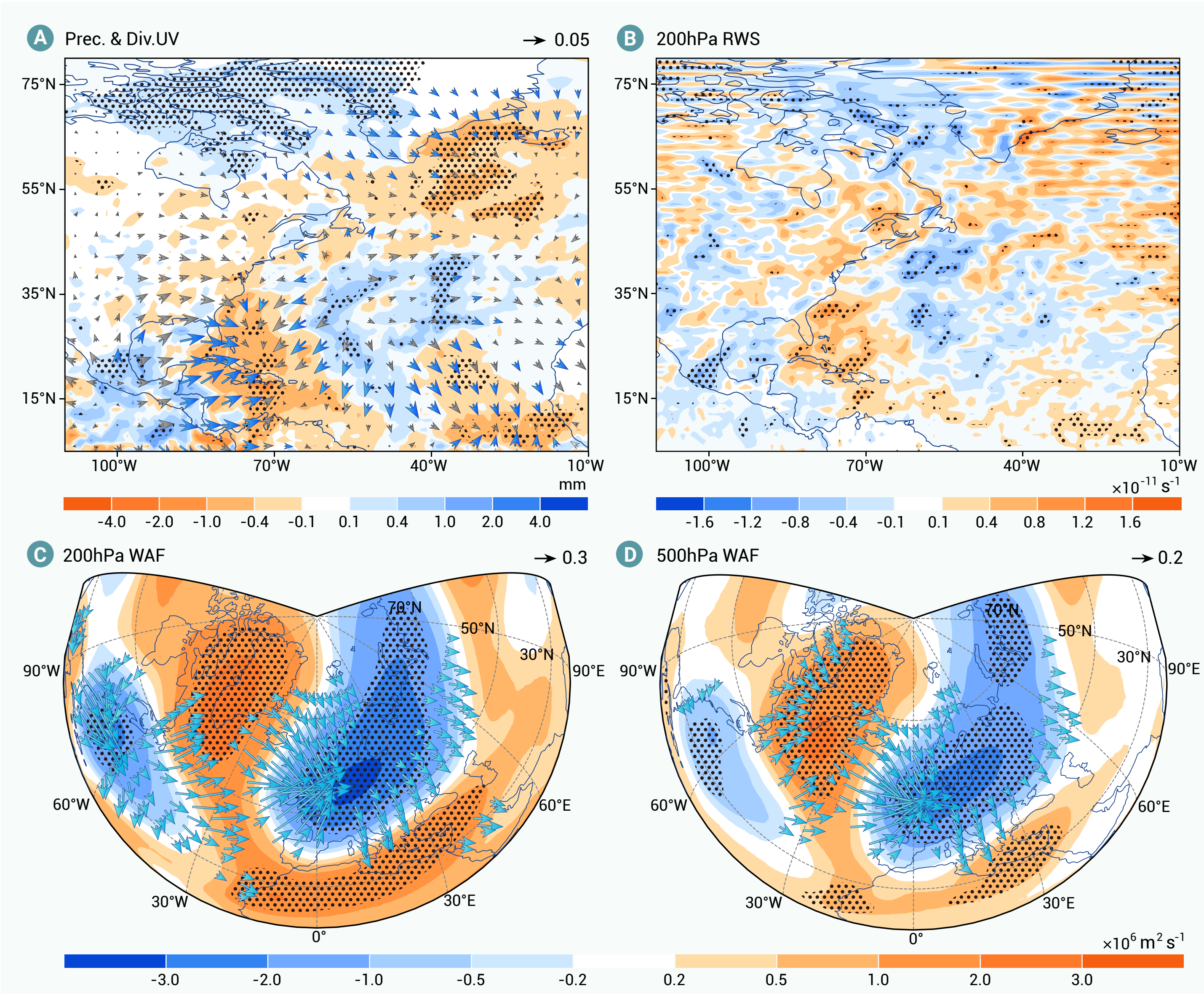

Figure 3. The precipitation, divergence winds and Rossby wave activity flux associated with the North Atlantic (NA) tropical cyclone activities The spatial distribution of (A) total precipitation (shading, unit: mm) and 200 hPa divergence wind (arrow, unit: m s^{-1}), (B) the Rossby wave source (shading, unit: s^{-2}) at 200 hPa, (C) the stream function (shading, unit: m^2 s^{-1}) and wave activity flux (arrow, unit: m^2 s^{-2}) at 200 hPa, (D) the stream function (shading, unit: m^2 s^{-1}) and wave activity flux (arrow, unit: m^2 s^{-2}) at 500 hPa in October based on the ERA5 reanalysis datasets (1982–2020) regressed onto the NA accumulated cyclone energy (ACE) principal mode time series. The effects of ENSO in September are eliminated in all regression fields. The dotted areas, the blue arrows represent statistical significance at the 90% confidence level by a two-tailed Student's *t*-test.

located in the KLS, greater than 0.5 ($p < 0.001$; Figure 2A). Apart from that, negative correlations exist in a few regions, located in the Beaufort Sea and the Canadian Arctic Archipelago, in agreement with the findings by Scoccimarro et al.[45] To determine the causal relationship between the NA TC activity and KLS SIC, we quantify the causality information from the NA ACE in late September to the KLS SIC in October using the Liang-Kleeman information flow diagnostics. The spatial distribution of the information flow is basically consistent with that of the correlation analysis (Figure 2B), confirming unidirectional causality from the NA ACE to Arctic SIC, with peak causality information over the Laptev Sea. This reinforces that the NA TC activity can be a potential driver of KLS sea ice positive anomalies. Moreover, singular value decomposition (SVD) analysis isolates coupled variability modes between the NA ACE index in late September and the KLS SIC in October. The principal SVD mode captures a statistically significant covariance structure, explaining 42.0% of the joint variability (Figures 2C–D). Specifically, positive ACE anomalies in the NA covary coherently with SIC increases across the KLS, with a time-series correlation coefficient of 0.68 ($p < 0.001$; Figure 2E). This observational evidence clearly demonstrates a positive correlation between NA ACE and KLS SIC, implying that atmospheric teleconnection may play an important role.

Mechanism linking the NA TC activity to the KLS sea ice

Enhanced NA TC activity during late summer-early autumn can initiate a cascading atmospheric response through diabatic heating-driven mechanisms. Regression analyses with the NA ACE index show that the NA TC activity in late September leads to a significant enhancement of tropical convective precipitation in the subtropical NA (near 25°N–40°N), along with anomalous divergence in the upper troposphere (200 hPa) (Figure 3A). The anomalies of the local divergent wind and neighboring convergent motion may related to the latent heat release associated with TC activity. A localized Rossby wave source (RWS) is centered near 30°N, 55°W (Figure 3B) due to the pronounced negative vorticity tendencies over the NA (Figure S1). The dominant RWS aligns with TC-induced divergent convective outflow, which excites barotropic energy conversion (Figure S2), facilitating wave energy dispersion to the northeastward. Rossby wave activity fluxes at both 200 hPa and 500 hPa exhibit that the planetary-scale Rossby wave trains originate in the NA, where the TC activity is highly active, and then propagate coherently northeastward. It is characterized by a northeastward propagation from the

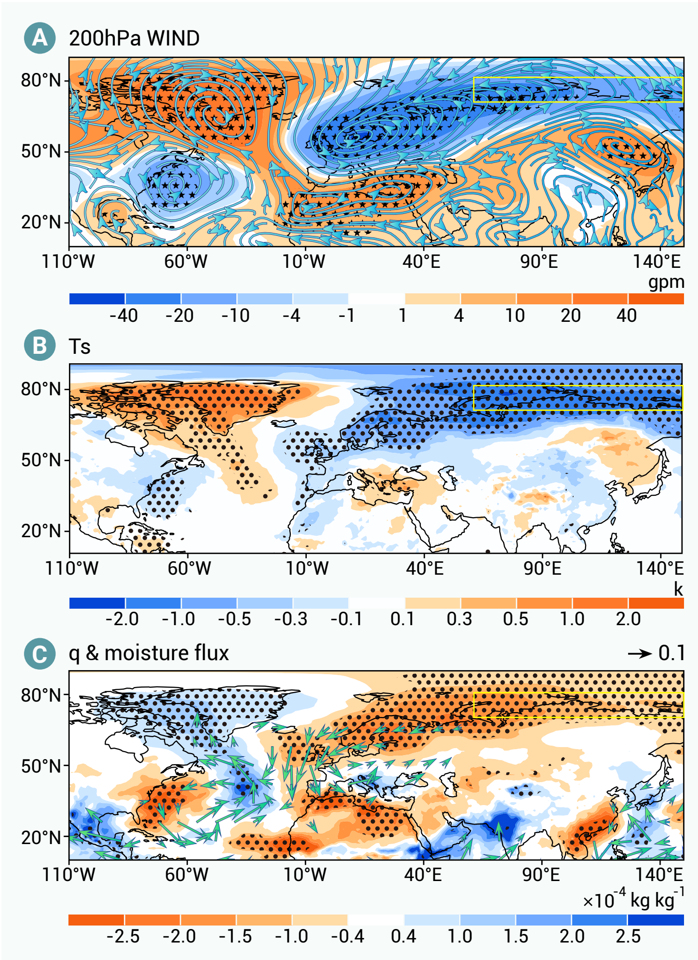

Figure 4. The atmospheric circulation and thermodynamic variables associated with the North Atlantic (NA) tropical cyclone activities (A) 200 hPa Geopotential height (shading, unit: gpm) and wind (streamlines), (B) surface temperature (shading, unit: K), (C) specific humidity (shading, unit: kg kg^{-1}) and vertically integrated moisture flux (arrow, unit: kg m^{-1} s^{-1}) in lower-tropospheric (1000–850 hPa) in October based on the ERA5 reanalysis datasets (1982–2020) regressed onto the NA accumulated cyclone energy principal mode time series. The effects of ENSO in September are eliminated in all regression fields. The yellow box shows the Kara-Laptev Seas, the dotted areas and green arrows represent statistical significance at the 90% confidence level by a two-tailed Student's *t*-test.

NA to the vicinity of Greenland, and then southeastward propagation to Europe (Figures 3C–D), in general agreement with the recognized path of the great circle.[62]

Regression analyses of October atmospheric circulation patterns against the late September NA ACE index are further analyzed as shown in Figure 4A. The atmospheric circulation anomalies exhibit a quasi-barotropic structure consistent with the Rossby wave trains, characterized by an anomalous cyclonic circulation in the NA, an anomalous anticyclonic circulation over Greenland, and an anomalous cyclonic circulation over Europe extending northeastward into the KLS (Figures 4A & S3). The mid- and upper-level cyclonic circulation anomalies over the KLS region related to the NA TC activity cause large-scale ascending motions (negative Omega values) over much of the KLS region (Figure S4). This anomalous ascending, driven by low-level convergence and upper-level divergence, suppresses the climatology subsidence normally observed in October, thereby suppressing the adiabatic warming effect,[63–65] and ultimately driving the pronounced surface cooling over the KLS region (Figure 4B), which creates thermally favorable conditions for sea ice increases there (Figures 2A & D). Concurrently, diminished poleward meridional moisture transport from mid-latitudes reduces lower-tropospheric specific humidity at the KLS, creating a drier atmosphere with reduced atmospheric water vapor content (Figure 4C). The resulting drier conditions enhance evaporation from open water, which absorbs substantial latent heat, leading to a pronounced decrease in sea surface temperature and accelerating seawater freezing into sea ice.[66] These colder and drier atmospheric conditions are conducive to promoting sea ice production and facilitating the maintenance of sea ice, leading to enhancements in sea ice over the KLS (Figures 2A & D). This mechanism demonstrates reverse consistency with established research findings regarding how local anomalous atmospheric circulation modulates Arctic sea ice variability, specifically, the established insights that anomalous anticyclonic circulation amplifies regional winter warming and sea ice loss through poleward heat and moisture advection coupled with adiabatic heating.[22,67]

Atmospheric model experiments for the teleconnection associated with the NA TC activity

Figure 5 presents atmospheric circulation and thermodynamic variables anomalies in October derived from the difference between ANOM and CTRL simulations of CAM6. The model reproduces the teleconnection mechanism bridging the NA and the KLS regions by superimposing anomalous atmospheric circulation patterns associated with the TC activity over the NA in late September. Composite anomalies depict a coherent tripole anomalous circulation pattern, featuring an anomalous cyclonic center over the North Atlantic, an anomalous anticyclonic center on Greenland, and an anomalous cyclonic spanning from Europe to the Laptev Sea (Figures 5A & S5A–B), which is consistent with the observation of Figures 4A & S3. Moreover, the CAM6 outputs demonstrate planetary-scale Rossby wave propagation along a path from the NA to the Arctic at both 200 hPa and 500 hPa (Figures 5B & S5c), exhibiting spatial congruence with observational patterns (Figures 3C–D). Notably, the simulated surface temperature reductions and lower-tropospheric drying over the KLS also align with observations (Figures 4B–C), though the model exhibits marginally amplified magnitudes compared to reanalysis data (Figures 5C–D). These substantiate a dynamical pathway that establishes a relationship between the KLS atmospheric circulation and the NA tropical system, where TC activity, as a contributor to the RWS, can trigger barotropic Rossby wave trains propagating northeastward, eventually establishing anomalous cyclonic over the KLS. This local cyclonic circulation pattern suppresses adiabatic heating through enhanced ascending motion while impeding meridional moisture flux, collectively leading to thermodynamic conditions conducive to sea ice increase in October. The model-observation consistency reveals the robustness of the link between the tropical system and the local anomalous atmospheric circulation over the Arctic. Supplementary sensitivity experiments forcing with TC-related tropospheric temperature anomalies (300–850 hPa) yield nearly identical circulation and thermodynamic responses over the KLS (Figure S6), confirming that the teleconnection signal is robust regardless of whether SLP or heating-related temperature anomalies are used to represent TC activity.

DISCUSSION AND CONCLUSION

The KLS, as the critical "ice factory" in the Arctic, is significantly affected by tropical systems through the tropical-Arctic atmospheric linkage. This study elucidates the mechanism through which NA TC activity in late summer can affect KLS sea ice in October. Observational analyses give robust positive correlations between the late September ACE over the NA and October SIC over the KLS, and confirm that the SIC anomaly lags about 20 days behind the anomalous ACE. The frequent NA TC-induced diabatic heating generates RWS, triggering northeastward-propagating barotropic Rossby wave trains. This teleconnection establishes a quasi-barotropic tripole circulation pattern characterized by anomalous cyclonic over the NA, anomalous anticyclonic over Greenland, and anomalous cyclonic extending from Europe to the KLS. Then, the anomalous cyclonic over the KLS suppresses adiabatic warming through attenuating subsidence motions, and reduces meridional moisture flux, which collectively reinforce colder and drier atmospheric conditions conducive to sea ice growth. These findings align with recent studies linking anomalous cyclonic (anticyclonic) circulation to increased (decreased) Arctic sea ice.[22,68,69] The CAM6 model can replicate the observed teleconnection, capturing the anomalous tripole circulation structure and planetary-scale Rossby wave propagation. Although the model slightly overestimates thermodynamic effects, it does reproduce the spatial structure of the anomalous temperature and humidity fields that favor the increase of sea ice over the KLS when strong ACE appears over NA.

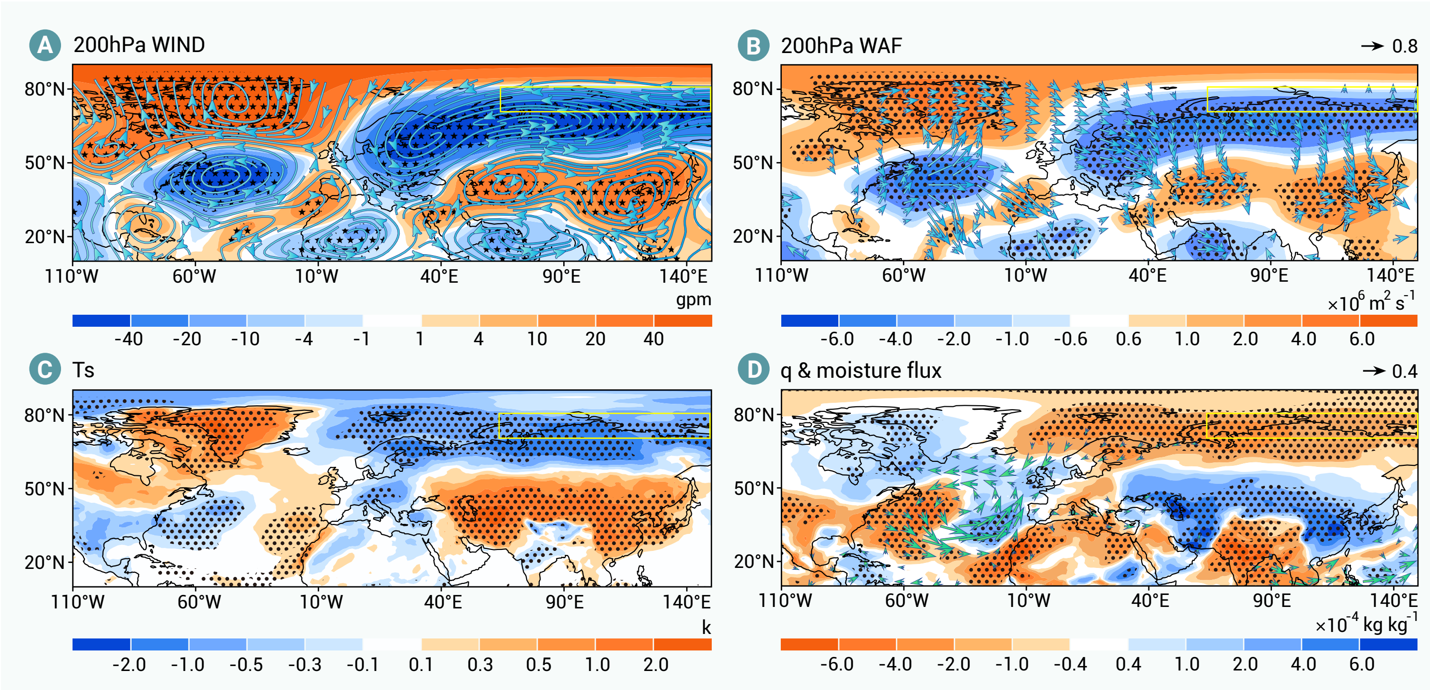

Figure 5. Ensemble mean anomalies of atmospheric circulation and thermodynamic variables simulated by the Community Atmosphere Model version 6 (CAM6) The anomalies of (A) 200 hPa geopotential height (shading, unit: gpm) and wind (streamline), (B) the 200 hPa stream function (shading, unit: m^2 s^{-1}) and wave activity flux (arrow, unit: m^2 s^{-2}), (C) the surface temperature (shading, unit: K), (D) specific humidity (shading, unit: kg kg−1) and vertically integrated moisture flux (arrow, unit: kg m^{-1} s^{-1}) in lower-tropospheric (1000–850 hPa) between the ANOM simulations and CTRL simulations (ANOM minus CTRL). The yellow box represents the Kara-Laptev Seas, the dotted areas, green and blue arrows show statistical significance at the 90% confidence level by a two-tailed Student's *t*-test.

Scoccimarro et al.[45] investigated a negative correlation between sea ice in the Beaufort Sea and NA TC activity, in addition to showing the positive correlation between the KLS sea ice and NA TC activity. The minor differences in intensity of the correlation between their study and our study probably stem from differences in the temporal scales analyzed. For example, their study focuses on the synchronous correlation in September of 1979–2006, whereas our study quantifies the correlation between TC activity in late September and sea ice lagged about 20 days over the period 1982–2020. This lagged relationship is more significant than the synchronous relationship. At the same time, this lead-lag relationship also emphasizes the possible causal link between the NA TC activity and KLS SIC.

Our prior study demonstrated that the WNP TC activity drives increased SIC in the Arctic-Pacific sector with a lag of approximately 30 days.[41] In contrast, this study reveals that NA TC activity precedes KLS SIC by about 20 days. While both linkages are mediated by TC-excited Rossby waves propagating northeastward, the difference in lag duration is likely attributable to disparities in Rossby wave propagation pathways. Specifically, Rossby waves triggered by NA TC activity originate near the NA (35°N, 60°W) and traverse a notably shorter pathway (4,700 km) along a relatively direct route: northeastward to Greenland, then southeastward to Europe. This trajectory aligns with the high-latitude waveguide, promoting efficient energy dispersion. Conversely, waves excited by the WNP TC activity follow a longer, more circuitous trajectory (7,000 km), propagating poleward across the North Pacific, reaching the Bering Strait, and finally penetrating the Arctic-Pacific sector. Besides, other factors may contribute to this lag difference. The NA conditions in the peak TC season of late September feature strengthened midlatitude westerlies, potentially accelerating wave propagation compared to mid-August WNP conditions. This background flow modulation in the NA pathway may exploit a more barotropic stable waveguide, reducing energy dissipation versus the trans-Pacific route, which intersects regions of stronger baroclinicity.

These distinctions in propagation geometry, compounded by seasonal circulation contrasts, collectively contribute to the observed 10-day differential in teleconnection lags. It's worth noting that our findings on poleward-propagating Rossby waves do not contradict the conventional view that TC typically excites southeastward-propagating Rossby. While a single TC typically excites southeastward waves, multiple TC forcings under high-ACE conditions may generate distinct "great circle" patterns through wave superposition and background flow interactions, resulting in poleward wave propagation. Future work should quantify the relative roles of pathway length versus atmospheric state in modulating Rossby wave transit times. Additionally, future work could integrate high-resolution ocean-ice components, enhance the ability of numerical models to resolve TC characteristics (intensity, track, duration) and their nonlinear interactions with the Arctic, particularly as greenhouse forcing accelerates TC poleward migration and intensification.[70–72] As anthropogenic warming amplifies the NA TC intensity.[44] and northeastward migration,[43] and this may have enhanced the Arctic-tropical teleconnection, which further has a more pronounced effect on the KLS sea ice, and thus the relationship between the NA TC activity and the Arctic sea ice warrants further study.

REFERENCES

1. Cavalieri D. J. and Parkinson C. L. (2012). Arctic sea ice variability and trends, 1979–2010. *The Cryosphere* **6**:881–889. DOI:10.5194/tc-6-881-2012
2. Yadav J., Kumar A. and Mohan R. (2020). Dramatic decline of Arctic sea ice linked to global warming. *Nat. Hazards* **103**:2617–2621. DOI:10.1007/s11069-020-04064-y
3. Reimnitz E., Dethleff D. and Nürnberg D. (1994). Contrasts in Arctic shelf sea-ice regimes and some implications: Beaufort Sea versus Laptev Sea. *Mar. Geol.* **119**:215–225. DOI:10.1016/0025-3227(94)90182-1
4. Cornish S. B., Johnson H. L., Mallet R. D. C., et al. (2022). Rise and fall of sea ice production in the Arctic Ocean's ice factories. *Nat. Commun.* **13**:7800. DOI:10.1038/s41467-022-34785-6
5. Zhang A., Yi D. L. and Fan K. (2024). Nonstationary thermodynamic and dynamic contributions to the interannual variability of winter sea ice growth in the Kara–Laptev Seas. *Environ. Res. Lett.* **19**:064067. DOI:10.1088/1748-9326/ad4fa4
6. Wang S., Nath D. and Chen W. (2021). Nonstationary relationship between sea ice over Kara–Laptev seas during August–September and Ural blocking in the following winter. *Int. J. Climatol.* **41**:E1608–E1622. DOI:10.1002/joc.6794
7. Cohen J., Agel L., Barlow M., et al. (2021). Linking Arctic variability and change with extreme winter weather in the United States. *Science* **373**:1116–1121. DOI:10.1126/science.abi9167
8. Zhang P., Wu Y., Simpson I. R., et al. (2018). A stratospheric pathway linking a colder Siberia to Barents-Kara Sea sea ice loss. *Sci. Adv.* **4**:eaat6025. DOI:10.1126/sciadv.aat6025
9. Zhang R. and Screen J. A. (2021). Diverse Eurasian winter temperature responses to Barents-Kara sea ice anomalies of different magnitudes and seasonality. *Geophys.*

Res. Lett. 48:e2021GL092726. DOI:10.1029/2021GL092726

10. Guo H., Yi Z., Xu T., et al. (2024). Different responses of surface air temperature over Eurasia in early and late winter to the autumn Kara–Laptev Sea ice. *Environ. Res. Lett.* 19:044042. DOI:10.1088/1748-9326/ad345f
11. Kim B.-M., Son S.-W., Min S.-K., et al. (2014). Weakening of the stratospheric polar vortex by Arctic sea-ice loss. *Nat. Commun.* 5:4646. DOI:10.1038/ncomms5646
12. Li F. and Wang H. (2012). Autumn sea ice cover, winter Northern hemisphere annular mode, and winter precipitation in Eurasia. *J. Clim.* 26:3968–3981. DOI:10.1175/JCLI-D-12-00380.1
13. Chen S., Chen W., Zhou W., et al. (2024). Interdecadal variation in the impact of Arctic sea ice on El Niño–Southern Oscillation: The role of atmospheric mean flow. *J. Clim.* 37:5483–5506. DOI:10.1175/JCLI-D-23-0733.1
14. Chen S., Chen W., Wu R., et al. (2025). Asymmetric impacts of Arctic sea ice anomalies on El Niño-Southern Oscillation. *Npj Clim. Atmospheric Sci.* 8:276. DOI:10.1038/s41612-025-01168-9
15. Cheng X., Chen S., Chen W., et al. (2025). Influence of winter Arctic sea ice anomalies on the following autumn Indian Ocean dipole development. *J. Clim.* 38:3109–3129. DOI:10.1175/JCLI-D-24-0419.1
16. Chen S., Chen W., Yu B., et al. (2023). Impact of the winter Arctic sea ice anomaly on the following summer tropical cyclone genesis frequency over the western North Pacific. *Clim. Dyn.* 61:3971–3988. DOI:10.1007/s00382-023-06789-5
17. Baxter I., Ding Q., Schweiger A., et al. (2019). How tropical pacific surface cooling contributed to accelerated sea ice melt from 2007 to 2012 as ice is thinned by anthropogenic forcing. *J. Clim.* 32:8583–8602. DOI:10.1175/JCLI-D-18-0783.1
18. Ding Q., Wallace J. M., Battisti D. S., et al. (2014). Tropical forcing of the recent rapid Arctic warming in northeastern Canada and Greenland. *Nature* 509:209–212. DOI:10.1038/nature13260
19. Meehl G. A., Chung C. T. Y., Arblaster J. M., et al. (2018). Tropical decadal variability and the rate of Arctic sea ice decrease. *Geophys. Res. Lett.* 45:11,326–11,333. DOI:10.1029/2018GL079989
20. Clancy R., Bitz C. and Blanchard-Wrigglesworth E. (2021). The influence of ENSO on Arctic sea ice in large ensembles and observations. *J. Clim.* 34:9585–9604. DOI:10.1175/JCLI-D-20-0958.1
21. Liu J., Curry J. A. and Hu Y. (2004). Recent Arctic sea ice variability: Connections to the Arctic Oscillation and the ENSO. *Geophys. Res. Lett.* 31:L09211. DOI:10.1029/2004GL019858
22. Hu, C., Yang, S., Wu, Q., et al. (2016). Shifting El Niño inhibits summer Arctic warming and Arctic sea-ice melting over the Canada Basin. *Nat. Commun.* 7:11721. DOI:10.1038/ncomms11721
23. Luo, B., Luo, D., Ge, Y., et al. (2023). Origins of Barents-Kara sea-ice interannual variability modulated by the Atlantic pathway of El Niño–Southern Oscillation. *Nat. Commun.* 14:585. DOI:10.1038/s41467-023-36136-5
24. Zhou B., Song Z., Yin Z., et al. (2024). Recent autumn sea ice loss in the eastern Arctic enhanced by summer Asian-Pacific Oscillation. *Nat. Commun.* 15:2798. DOI:10.1038/s41467-024-47051-8
25. Årthun M., Eldevik T., Smedsrud L. H., et al. (2012). Quantifying the influence of Atlantic heat on Barents sea ice variability and retreat. *J. Clim.* 25:4736–4743. DOI:10.1175/JCLI-D-11-00466.1
26. Polyakov I. V., Pnyushkov A. V., Alkire M. B., et al. (2017). Greater role for Atlantic inflows on sea-ice loss in the Eurasian Basin of the Arctic Ocean. *Science* 356:285–291. DOI:10.1126/science.aai8204
27. Woods C. and Caballero R. (2016). The role of moist intrusions in winter Arctic warming and sea ice decline. *J. Clim.* 29:4473–4485. DOI:10.1175/JCLI-D-15-0773.1
28. Hofsteenge M. G., Graversen R. G., Rydsaa J. H., et al. (2022). The impact of atmospheric Rossby waves and cyclones on the Arctic sea ice variability. *Clim. Dyn.* 59:579–594. DOI:10.1007/s00382-022-06145-z
29. Matsumura S. and Kosaka Y. (2019). Arctic–Eurasian climate linkage induced by tropical ocean variability. *Nat. Commun.* 10:3441. DOI:10.1038/s41467-019-11359-7
30. Xie Y., Duan A., Zhang C., et al. (2025). Reversed link between central pacific ENSO and Greenland–Barents sea ice. *Npj Clim. Atmospheric Sci.* 8:1–7. DOI:10.1038/s41612-025-00912-5
31. Sheng Z., He Y., Wang S., et al. (2025). Dynamics, chemistry, and modeling studies in the aviation and aerospace transition zone. *The Innovation* 6:101012. DOI:10.1016/j.xinn.2025.101012
32. Finocchio P. M. and Doyle J. D. (2019). How the speed and latitude of the jet stream affect the downstream response to recurving tropical cyclones. *Mon. Weather Rev.* 147:3261–3281. DOI:10.1175/MWR-D-19-0049.1
33. Sardeshmukh P. D. and Hoskins B. J. (1988). The generation of global rotational flow by steady idealized tropical divergence. *J. Atmospheric Sci.* 45:1228–1251. DOI:10.1175/1520-0469(1988)045<1228:TGOGRF>2.0.CO;2
34. Li T. and Fu B. (2006). Tropical cyclogenesis associated with rossby wave energy dispersion of a preexisting typhoon. Part I: Satellite data analyses. *J. Atmospheric Sci.* 63:1377–1389. DOI:10.1175/JAS3692.1
35. Li T., Ge X., Wang B., et al. (2006). Tropical cyclogenesis associated with rossby wave energy dispersion of a preexisting typhoon. Part II: Numerical simulations. *J. Atmospheric Sci.* 63:1390–1409. DOI:10.1175/JAS3693.1
36. Ge X., Li T. and Peng M. S. (2010). Cyclogenesis simulation of typhoon prapiroon (2000) associated with rossby wave energy dispersion. *Mon. Weather Rev.* 138:42–54. DOI:10.1175/2009MWR3005.1
37. Fan X., Li Y., Wei N., et al. (2024). Rossby wave amplified by tropical cyclones over the bay of bengal and its downstream impact on precipitation in South China. *Geophys. Res. Lett.* 51:e2023GL107208. DOI:10.1029/2023GL107208
38. Kawamura R. and Ogasawara T. (2006). On the role of typhoons in generating PJ teleconnection patterns over the western north Pacific in late summer. *Sola* 2:37–40. DOI:10.2151/sola.2006-01039
39. Riboldi J., Grams C. M., Riemer M., et al. (2019). A phase locking perspective on rossby wave amplification and atmospheric blocking downstream of recurving western North Pacific tropical cyclones. *Mon. Weather Rev.* 147:567–589. DOI:10.1175/MWR-D-18-0271.1
40. Villarini G., Vecchi G. A. and Scoccimarro E. (2025). Tropical cyclones and associated impacts: A global perspective (Elsevier Press). DOI:10.1016/C2021-0-02882-0
41. Zeng L., Ha Y., Zhao C., et al. (2024). Tropical cyclone activity over western North Pacific favors Arctic sea ice increase. *Nat. Commun.* 15:9564. DOI:10.1038/s41467-024-53991-y
42. Zeng L., Ha Y., Zhao C., et al. (2025). Possible effects of tropical cyclone activities over eastern North Pacific on Arctic sea ice. *Environ. Res. Lett.* 20:094020. DOI:10.1088/1748-9326/adf56b
43. Murakami H. and Wang B. (2010). Future change of North Atlantic tropical cyclone tracks: Projection by a 20-km-mesh global atmospheric model. *J. Clim.* 23:2699–2721. DOI:10.1175/2010JCLI3338.1
44. Villarini G. and Vecchi G. A. (2013). Projected increases in North Atlantic tropical cyclone intensity from CMIP5 Models. *J. Clim.* 26:3231–3240. DOI:10.1175/JCLI-D-12-00441.1
45. Scoccimarro E., Gualdi S. and Navarra A. (2012). Tropical cyclone effects on Arctic sea ice variability. *Geophys. Res. Lett.* 39:L17704. DOI:10.1029/2012GL052987
46. Knapp K. R., Kruk M. C., Levinson D. H., et al. (2010). The international best track archive for climate stewardship (IBTrACS): Unifying tropical cyclone data. *Bull. Am. Meteorol. Soc.* 91:363–376. DOI:10.1175/2009BAMS2755.1
47. Waple A. M., Lawrimore J. H., Halpert M. S., *et al.* (2002). Climate assessment for 2001. *Bull. Am. Meteorol. Soc.* 83:S1–S62. http://www.jstor.org/stable/26215369
48. Reynolds R. W., Smith T. M., Liu C., et al. (2007). Daily high-resolution-blended analyses for sea surface temperature. *J. Clim.* 20:5473–5496. DOI:10.1175/2007JCLI1824.1
49. Hersbach H., Bell B., Berrisford P., et al. (2020). The ERA5 global reanalysis. *Q. J. R. Meteorol. Soc.* 146:1999–2049. DOI:10.1002/qj.3803
50. Rayner N. A., Parker D. E., Horton E. B., et al. (2003). Global analyses of sea surface temperature, sea ice, and night marine air temperature since the late nineteenth century. *J. Geophys. Res. Atmospheres* 108:2002JD002670. DOI:10.1029/2002JD002670
51. Beer C., Reichstein M., Tomelleri E., et al. (2010). Terrestrial gross carbon dioxide uptake: Global distribution and covariation with climate. *Science* 329:834–838. DOI:10.1126/science.1184984
52. Peng S., Piao S., Ciais P., et al. (2013). Asymmetric effects of daytime and night-time warming on Northern Hemisphere vegetation. *Nature* 501:88–92. DOI:10.1038/nature12434
53. An S.-I. (2003). Conditional maximum covariance analysis and its application to the tropical Indian Ocean SST and surface wind stress anomalies. *J. Clim.* 16:2932–2938. DOI:10.1175/1520-0442(2003)016<2932:CMCAAI>2.0.CO;2
54. Zhang L., Ren X., Cai W., et al. (2024). Weakened western Indian Ocean dominance on Antarctic sea ice variability in a changing climate. *Nat. Commun.* 15:3261. DOI:10.1038/s41467-024-47655-0
55. Plumb R. A. (1985). On the three-dimensional propagation of stationary waves. *J. Atmospheric Sci.* 42:217–229. DOI:10.1175/1520-0469(1985)042<0217:OTTDPO>2.0.CO;2
56. Holton J. R. and Hakim G. J. (2013). An introduction to dynamic meteorology (Academic Press). DOI:10.1016/C2009-0-63394-8
57. Trenberth K. E., Branstator G. W., Karoly D., et al. (1998). Progress during TOGA in understanding and modeling global teleconnections associated with tropical sea surface temperatures. *J. Geophys. Res. Oceans* 103:14291–14324. DOI:10.1029/97JC01444
58. Liang X. S. (2018). Causation and information flow with respect to relative entropy. *Chaos Interdiscip. J. Nonlinear Sci.* 28:075311. DOI:10.1063/1.5010253
59. Bretherton C. S., Smith C. and Wallace J. M. (1992). An intercomparison of methods for finding coupled patterns in climate data. *J. Clim.* 5:541–560. DOI:10.1175/1520-0442(1992)005<0541:AIOMFF>2.0.CO;2
60. Wallace J. M., Smith C. and Bretherton C. S. (1992). Singular value decomposition of wintertime sea surface temperature and 500-mb height anomalies. *J. Clim.* 5:561–576. DOI:10.1175/1520-0442(1992)005<0561:SVDOWS>2.0.CO;2
61. Bogenschutz P. A., Gettelman A., Hannay C., et al. (2018). The path to CAM6: Coupled simulations with CAM5.4 and CAM5.5. *Geosci. Model Dev.* 11: 235–255. DOI:10.5194/gmd-11-235-2018
62. Hoskins B. J. and Karoly D. J. (1981). The steady linear response of a spherical atmosphere to thermal and orographic forcing. *J. Atmospheric Sci.* 38:1179–1196. DOI:10.1175/1520-0469(1981)038<1179:TSLROA>2.0.CO;2
63. Ding ., Schweiger A., L'Heureux M., et al. (2017). Influence of high-latitude atmospheric circulation changes on summertime Arctic sea ice. *Nat. Clim. Change*

7:289–295. DOI:10.1038/nclimate3241
64. Liu Z., Risi C., Codron F., et al. (2025). Anthropogenic intensification of Arctic anticyclonic circulation. *Sci. Adv.* **11**:eads4508. DOI:10.1126/sciadv.ads4508
65. Wernli H and Papritz L. (2018). Role of polar anticyclones and mid-latitude cyclones for Arctic summertime sea-ice melting. *Nat. Geosci.* **11**:108–113. DOI:10.1038/s41561-017-0041-0
66. Guo S., Chen R, Han C., et al. (2021). Five-year analysis of evaposublimation characteristics and its role on surface energy balance SEB on a midlatitude continental glacier. *Earth Space Sci.* **8**:e2021EA001901. DOI:10.1029/2021EA001901
67. Ding Q., Schweiger A., L'Heureux M., et al. (2019). Fingerprints of internal drivers of Arctic sea ice loss in observations and model simulations. *Nat. Geosci.* **12**:28–33. DOI:10.1038/s41561-018-0256-8
68. Baxter I. and Ding Q. (2022). An optimal atmospheric circulation mode in the Arctic favoring strong summertime sea ice melting and ice–albedo feedback. *J. Clim.* **35**:6627–6645. DOI:10.1175/JCLI-D-21-0679.1
69. Huang Y., Ding Q., Dong X., et al. (2021). Summertime low clouds mediate the impact of the large-scale circulation on Arctic sea ice. *Commun. Earth Environ.* **2**:1–10. DOI:10.1038/s43247-021-00114-w
70. Elsner J. B., Kossin J. P. and Jagger T. H. (2008). The increasing intensity of the strongest tropical cyclones. *Nature* **455**:92–95. DOI:10.1038/nature07234
71. Studholme J., Fedorov A. V., Gulev S. K., et al. (2022). Poleward expansion of tropical cyclone latitudes in warming climates. *Nat. Geosci.* **15**:14–28. DOI:10.1038/s41561-021-00859-1
72. Cao X., Watanabe M., Wu R.,et al. (2024). The projected poleward shift of tropical cyclogenesis at a global scale under climate change in MRI-AGCM3.2H. *Geophys. Res. Lett.* **51**:e2023GL107189. DOI:10.1029/2023GL107189

FUNDING AND ACKNOWLEDGMENTS

This research is jointly sponsored by the National Key Research and Development Program of China (grant 2022YFF0801702), the National Natural Science Foundation of China (grant 42575038, 41925022 and 42206257), and the Graduate Student Innovation Program of National University of Defense Technology (XJJC2025075). The funders had no role in study design, data collection and analysis, decision to publish, or preparation of the manuscript.

AUTHOR CONTRIBUTIONS

L. Z. and Y. Ha conceptualized the study, and both authors jointly analyzed the results. The model simulations were conducted in collaboration by L. Z., Y. Ha, and Z. Z., who also wrote the initial manuscript draft. C. Z., J. D., H. D., Y. Z., and Y. Hu. assisted with manuscript revisions, contributed to the writing and editing process, and offered valuable insights on the mechanisms discussed. All authors contributed to the manuscript and approved the final version.

DECLARATION OF INTERESTS

The authors declare no competing interests.

DATA AND CODE AVAILABILITY

Maximum sustained surface winds and locations of TC activities are accessible from IBTrACS at https://www.ncdc.noaa.gov/ibtracs/. Sea ice concentration data can be accessed from ftp://eclipse.ncdc.noaa.gov/pub/OI-daily-v2/ (last access: 20 May 2025). The anomalies of meteorological fields from 1982 to 2020 can be retrieved from Monthly ERA5 reanalysis data (DOI: 10.24381/cds.6860a573, last access: 20 May 2025). MERRA-2 data are available at the Modeling and Assimilation Data and Information Services Center (https://data.rda.ucar.edu/ds313.2/0.9x1.25, last access: 20 May 2025). Monthly Niño 3.4 SST Index can be accessed from https://psl.noaa.gov/data/timeseries/month/Nino34/ (last access: 20 Dec 2024). The CESM2 model is available for download at https://www.cesm.ucar.edu/models/cesm2 (last access: 20 May 2025).